A Thermal Imaging Methodology To Study Evaporation Kinetics in Mine Tailings

Josée Maurais[1], Étienne Beaumont[1], Joanick Bourret[1], Emrik Dauphinais[1], Nicolas-Alexandre Bouchard[2] and Patrick Ayotte[1]*

[1]Département de chimie, Université de Sherbrooke, Sherbrooke, J1K 2R1, CANADA

[2]Rio Tinto Alcan International Limited, 1955 boul. Mellon, Jonquière, G7S 4L2, CANADA

KEYWORDS. Evaporation kinetics, thermal imaging, mine tailings, effective diffusion coefficient, water transport mechanisms, evaporative fluxes, fugitive dust emissions, water adsorption on mineral surfaces, vapour diffusion in porous media, capillary flow in bauxite residues.

ABSTRACT

Predicting why, how, and when mine tailings disposal sites become prone to dust scattering events is often hampered by our limited understanding of the factors that affect the drying rates from their surface layers. As a case study, thermal imaging is demonstrated here to be a valuable tool to study the evaporation mechanisms and rates from bauxite residues as a function of their thickness and physicochemical properties, as well as environmental conditions. These investigations reveal their that late stage drying rates are limited by gas phase diffusion through the interstitial air within their internal microporosity. The smallness of the effective diffusion coefficient indicates that water adsorption on bauxite residues surfaces is the dominant phenomenon responsible for their slow water vapour transport kinetics, a phenomenon that ultimately controls their late stage drying rates, that is when dust scattering is most likely to occur. As such, application of this thermal imaging methodology in the field may also contribute to improve the accuracy of risk assessment protocols, support intervention and mitigation strategies, underpin optimization efforts for mining residues management, and improve forecasting of fugitive dust emissions from mine tailings by enabling more accurate predictions of the evolution in their surface drying state.

INTRODUCTION

Fugitive dust emissions emanating from mining residues can be a significant environmental concern facing tailing storage facilities, challenging their prevention and mitigation efforts that, as a result, become increasingly costly and labor intensive (Allan, 1995; Power, Gräfe, & Klauber, 2011). Unfortunately, forecasting and risk assessment efforts are hampered by our limited

understanding of the impact of meteorological conditions, as well as of mine tailings microstructural and physicochemical properties, on their drying mechanisms and rates.

To tackle this problem, a bauxite residues storage area (BRSA) was selected as a case study allowing meteorological records to be scrutinized in order to highlight the environmental conditions that led to, and triggered, past fugitive dust emission events (Maurais et al., 2018). This enabled the investigation of drying kinetics to be steered towards the most critical and relevant environmental parameters for laboratory studies. Numerous meteorological parameters are continuously monitored by a weather station nearby the selected BRSA namely, wind speed and direction, precipitations, as well as atmospheric temperature and relative humidity (RH). This latter was shown to be the most aggravating environmental parameter leading to dust particles scattering events (Maurais et al., 2018). Therefore, thermal imaging techniques were brought to bear on this issue by evaluating whether they could help quantify the evaporation kinetics of bauxite residues. They are demonstrated herein to be convenient and effective tools for investigation into evaporation rates that govern the drying process and to provide invaluable insight into the underlying water transport mechanisms (Fuchs & Tanner, 1967; Pfister, McDonnell, Hissler, & Hoffmann, 2010; Price, 1980).

Previously reported methods for measuring water contents, drying rates and evaporative fluxes from porous media include frequency/time-domain reflectometry (Topp & Davis, 1985; Wang, Xia, Wang, & Lu, 2012; Yu & Drnevich, 2004), dielectric permittivity measurements (Wang et al., 2012), ground penetrating radar dielectric constant measurements (Van Dam, 2014), electrical conductivity or resistivity (Brevik, Fenton, & Lazari, 2006; Sheets & Hendrickx, 1995), visual inspection of the evolution of the drying front within the sample (Shokri, Lehmann, & Or, 2009; Shokri & Or, 2011), heat-pulse probes (Bristow, 1998; Bristow, Campbell, & Calissendorff, 1993;

63 Hopmans, Šimunek, & Bristow, 2002), to name only but a few. Unfortunately, these methods
64 either lack the sensitivity or selectivity towards the surface layer, and/or cannot be easily deployed
65 for continuous in-situ monitoring and field applications (Amano & Salvucci, 1989). They are thus
66 unsuitable for the specific context of evaluating surface drying states and rates as part of risk
67 assessment protocols for dust emissions from BRSA. Thermal imaging techniques possess those
68 desirable attributes and may thus prove to be equally effective at probing drying kinetics under
69 controlled conditions in the laboratory, as well as providing a potentially powerful management
70 tool to characterize the evaporation rates from bauxite tailing surfaces at BRSA (Price, 1980).
71 Drying kinetics from porous materials are very complex, displaying contributions from a number
72 of different water transport mechanisms resulting in distinctive regimes and stages that all depend
73 sensitively on their water content, their microstructural and physicochemical properties, as well as
74 on environmental conditions (McKenna Neuman, Boulton, & Sanderson, 2009). Indeed, when the
75 water content is elevated, as in the early stages of drying, capillary flow is expected to dominate
76 water transport to the surface (a regime thereafter referred to as stage I) allowing large evaporation
77 fluxes from wet residues to be sustained (Neriah, Assouline, Shavit, & Weisbrod, 2014; Or,
78 Lehmann, Shahraeeni, & Shokri, 2006; Shahraeeni & Or, 2010; Teng, Zhang, Zhang, Zhao, &
79 Sheng, 2019; Thiery, Rodts, Weitz, & Coussot, 2017). Eventually, the rupture of the wetting layer
80 at the percolation threshold causes hydraulic discontinuity within the porous media (Moldrup,
81 Olesen, Komatsu, Schjønning, & Rolston, 2001). This shifts the limiting water transport
82 mechanism from capillary flow to gas phase diffusion thereby yielding a significant slowing down
83 of the evaporation rates (a regime thereafter referred to as stage II) (Griend & Owe, 1994; Or et
84 al., 2006; Saravanapavan & Salvucci, 2000). The water content at which the transition from stage
85 I to stage II occurs has been correlated to the microstructural features of the porous media (Shokri

& Or, 2011). Therefore, it is expected that the evaporation kinetics from bauxite tailings should not only depend strongly on their water content, but also on their chemical composition, as well as on their morphological and physicochemical properties, attributes that govern which water transport mechanism should be most effective under specific meteorological conditions (i.e., temperature and relative humidity) (Saravanapavan & Salvucci, 2000). Given the role of capillary forces in maintaining the cohesion of dust particles with tailing sites surfaces, forecasting of fugitive dust emissions from BRSA depend most critically on a detailed quantitative understanding of bauxite tailings evaporation kinetics as well as an the ability to predict their surface drying state (Shao, 2001).

In this work, we describe how thermal imaging techniques enable evaporation rates from bauxite residues to be quantified. This methodology should help describe, probe, understand, and predict bauxite residues evaporation kinetics, as well as their dependence on environmental parameters representative of those found at the BRSA (Neriah et al., 2014). Collectively, these investigations should improve our ability to predict the drying state of bauxite residues surfaces, forecast and prevent the occurrence of fugitive dust emissions, as well as devise efficient risk assessment and monitoring tools to assist in mining residues management and environmental mitigation efforts.

MATERIALS AND METHODS

A methodology based on thermal imaging techniques was devised allowing for the measurements of drying kinetics from porous media. The surface-sensitivity and selectivity of optical methods (i.e., tens to a few hundreds of microns) enable measurements of surface temperatures from mine tailings under controlled ambient temperature and relative humidity conditions in the laboratory. Furthermore, the portability and ease of use of the commercial

infrared camera used in this work (FLIR® Model A320) are attractive features for field applications. These may thus enable thermal imaging techniques to be brought to bear on real-time monitoring of the evaporation process from the surface of mine tailings storage facilities.

Under given environmental conditions (i.e., ambient T and RH), water vapour concentration and temperature gradients can establish rapidly in the superficial layers of evaporating porous media, evolving continuously thereafter throughout the drying process. These gradients provide a driving force for the long-range diffusive/convective transport of heat and water vapour, processes that are required to sustain water evaporation from the samples surface, and that explain the strong dependency of the drying kinetics on environmental parameters (Neriah et al., 2014). In addition, it is thus also expected that the drying kinetics should depend strongly on sample thickness, as well as on their microstructure and physico-chemical properties, in addition to their water content (Grifoll, Gastó, & Cohen, 2005). Under quasi-steady state conditions (Monteith, 1981), equation 1 indicates that the surface temperatures observed for evaporating bauxite residues can be understood by comparing the latent heat flux of evaporation from the samples surface (calculated from the evaporation flux, J_{evap}, and the vaporization enthalpy, ΔH_{evap}) to the sensible heat flux sustained by their thermal conductivity, K, through the gradient in their temperature depth-profile, ∇T (Kosky, Balmer, Keat, & Wise, 2013):

$$K \cdot \nabla T = J_{evap} \cdot \Delta H_{evap} \quad [1]$$

Therefore, surface temperature measurements can straightforwardly and directly inform on the evaporative fluxes emanating from drying mine tailings. The magnitude of evaporative cooling at the sample surface is reported using thermal imaging measurements of the difference in surface temperatures (ΔT, with a precision of ± 30 mK) between drying bauxite residues samples and those from reference samples. These latter are bauxite residues that have been let to reach equilibrium

with the environmental conditions, at the selected ambient temperature and relative humidity (Monteith, 1981).

Evaporation kinetics from porous media also depend strongly on their water content along with their physicochemical and morphological properties (Or et al., 2006). Indeed, at water contents above a critical threshold value, capillary flow supplies the evaporating surface with liquid water and is the dominant water transport mechanism that controls drying rates (Neriah et al., 2014). This critical threshold volumetric water content, θ_{thr}, is defined by the minimal water content for which long-range transport by solute diffusion in the liquid phase is possible (Moldrup et al., 2001; Shokri & Or, 2011; Thiery et al., 2017). Below θ_{thr}, the hydraulic continuity is disrupted, and the evaporation kinetics should thus become increasingly limited by water vapour diffusion from the vaporisation front to the sample's surface (Moldrup et al., 2001). Therefore, θ_{thr} informs us on the dominant transport mechanism likely to limit the evaporation of water and can be evaluated using a non-linear empirical relationship that relates θ_{thr} with the specific surface area (SSA) of the porous medium (Moldrup et al., 2001):

$$\theta_{thr} = 0.039 \cdot SSA_{vol}^{0.52} \quad [2]$$

Equation 2 indicates that materials with large SSAs, such as bauxite residue (44-87 cm^2/g) (Li, 1998, 2001; Li & Rutherford, 1996), yield in an elevated value of θ_{thr} expressed as V_w/V_t, where V_w is the volume of water and V_t the total volume of wet bauxite residues. Using the SSAs reported in the literature (Li, 1998, 2001; Li & Rutherford, 1996) along with the macroscopic densities measured for the bauxite residues used in the present study, ρ_{bulk} = (1.2 ± 0.1) g/cm^3, θ_{thr} is found to vary between 31 % and 44 %, with an average value of (38 ± 4) % (V_w/V_t).

The bauxite residue samples, having reached different drying stages, were collected from various locations at the selected BRSA. They were rinsed, dried and prepared with an initial solid fraction

155 of 70 % (m_b/m_t, where m_b is the mass of dry bauxite residues and m_t the total mass of wet bauxite
156 residues), an initial drying state representative of the late stages of drying where fugitive dust
157 emissions are most likely to occur. Furthermore, as it corresponds to an initial volumetric water
158 content of 37 %, a contribution from capillary flow driven evaporation (i.e., stage I) is therefore
159 likely to be observed in the early stages of the drying process for the experimental conditions
160 explored in this work. Subsequently, gas phase water diffusion and adsorption on bauxite residues
161 surfaces are expected to become the dominant mechanisms that should limit water transport from
162 the vaporisation plane to the evaporating samples' surface (i.e., stage II).

163 In order to provide insight into the conditions under which the diffusive and/or capillary
164 processes limit water transport to the surface and thus, the evaporation rate, sample holders with
165 various depths, d = 2, 4, 6, and 8 mm, were used. These thicknesses encompass the critical
166 superficial layers that are prone to dust scattering from BRSA surfaces. Surface temperature
167 measurements were performed using compacted samples of wet bauxite residues until completion
168 of water evaporation (i.e., when drying bauxite residues surface temperatures reach those of the
169 reference sample, within the thermal imaging temperature measurements accuracy of ± 30 mK).
170 Wet bauxite residues and reference samples were introduced in a controlled environmental
171 chamber (Humidity test chamber; VWR® Model 9005L), maintained at a fixed temperature and
172 ambient pressure (i.e., 310 K and 1 atm), and exposed to controlled relative humidity (RH)
173 conditions of 35 %, 40 %, 50 %, 60 % and 70 %. The thermal camera was placed in the
174 experimental chamber and was connected to a data processing software, allowing continuous and
175 simultaneous measurements of the reference and wet bauxite residues surface temperatures to be
176 performed for each sample thickness, as can been gleaned from the representative snapshots of a
177 typical experimental time series reported in Figure 1.

178 Finally, water adsorption isotherms were performed using initially dry bauxite residue
179 samples that have been let to equilibrate with the environmental conditions (i.e., T = 310 K, P = 1
180 atm, at the selected RHs). Once thermodynamic equilibrium was reached between the bauxite
181 residue sample and the selected environmental conditions, the gain in mass of the sample due to
182 the adsorbed water mass (m_w) was determined using a high precision analytical balance enabling
183 their equilibrium water content to be measured.
184

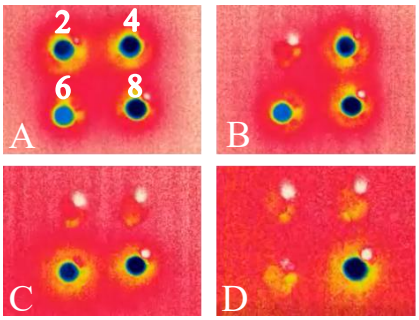

Figure 1. Snapshots from a time series showing thermal images of evaporating wet bauxite residue for sample thickness, d = 2 mm (top left), 4 mm (top right), 6 mm (bottom left) and 8 mm (bottom right) : as prepared **(A)**, and upon complete drying of the 2 mm **(B)**, 4 mm **(C)** and 6 mm **(D)** thick sample.

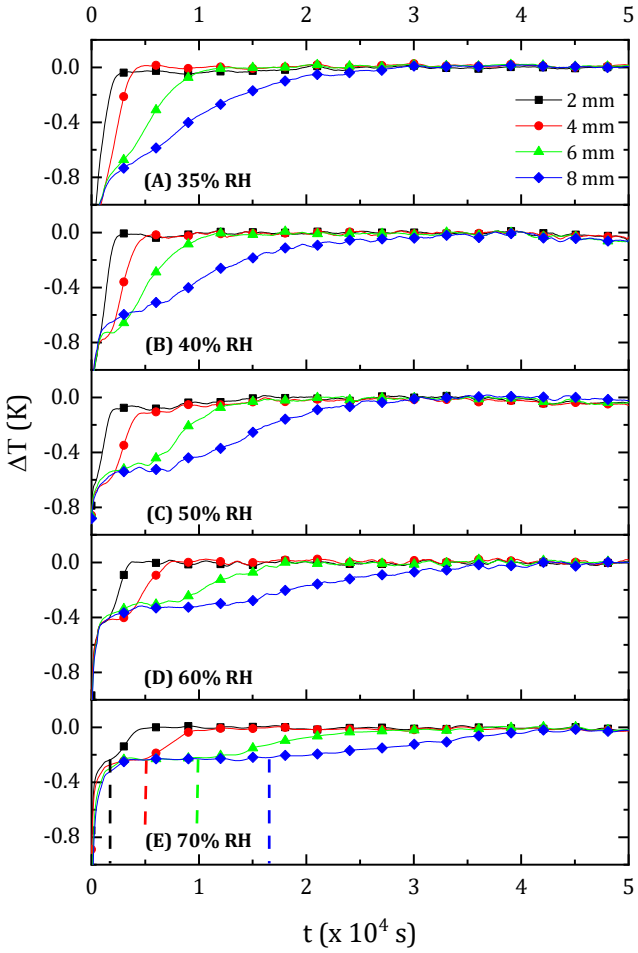

Figure 2. Evolution of the temperature difference (ΔT) between the sample and the reference surfaces during drying of bauxite residues prepared with an initial solid fraction of 70% (m_b/m_t) at T = 310 K. Sample thicknesses of 2 mm (black squares), 4 mm (red circles), 6 mm (green triangles) and 8 mm (blue diamonds) were monitored at a relative humidity of 35% (A), 40% (B), 50% (C), 60% (D) and 70% (E). The vertical lines in E indicate the onset of the transition from stage I to stage II evaporation regimes.

The evolution of the temperature difference between the bauxite residues and reference surfaces (ΔT) as a function of time for sample thicknesses, d = 2, 4, 6, and 8 mm (black squares, red circles, green triangle, and blue diamonds, respectively), at a selected relative humidity (RH = 35 %, 40 %, 50 %, 60 %, and 70 %, reported in Figure 2A, 2B, 2C, 2D, and 2E, respectively), reveals the complex nature of bauxite residues drying kinetics. As expected, the evaporation rates depend strongly, and in a non-linear way on d, indicating that long-range transport through the bauxite residues porous microstructure must play an essential role in the drying process. Lower initial ΔT values are observed for each RH in Figure 2, reported as $\Delta T_{free,\ evap.}$ increase from ~ -800 mK at 35 % RH to ΔT ~ -250 mK at 70 % RH appear to be conspicuously independent of d. This reveals that the initial drying rates remain constant during stage I evaporation, and that they recede as the ambient RH increases. This is most likely due to free water evaporation from wet bauxite residues in their early stages of drying, a process that is sustained by rapid capillary flow from the bulk to the surface (Or et al., 2006). As such, these initial ΔT value are reported as $\Delta T_{free,\ evap.}$ Figure 2 reveals that the duration of this capillary-driven free water evaporation regime increases with sample thickness and that it decreases with increasing RH.

Stage I evaporation is followed by an evaporation regime where surface temperatures slowly rise until the samples eventually reach thermal equilibrium with their environment. Indeed, as water content in evaporating bauxite residues decreases, it compromises the hydraulic continuity between the vaporisation plane, buried in the bulk of the sample, and their surface. Therefore, during stage II evaporation, the surface temperatures gradually rises as the evaporation rates become increasingly limited by the much slower diffusion of water vapour towards the sample surface until ΔT tends asymptotically to zero (i.e., near-equilibrium conditions). As a result, the dominant mechanism and rate-limiting process that sustains the evaporation flux from the samples

surface shifts from capillary flow (stage I) to diffusive water vapour transport (stage II). In Figure 2E, vertical dashed lines indicate the onset of the transition from stage I to stage II evaporation

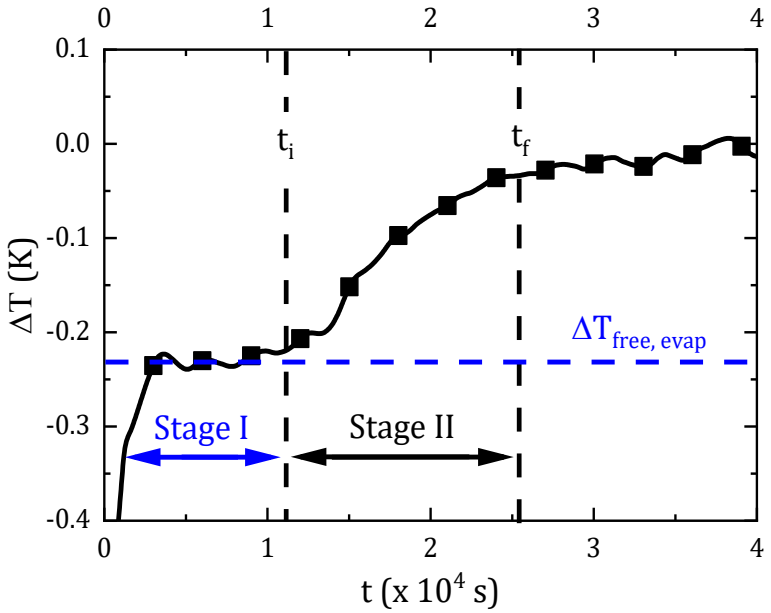

Figure 3. Evolution of the temperature difference (ΔT) between the sample and the reference surfaces during drying of a 6 mm thick bauxite residues sample with an initial solid fraction of 70% (m_b/m_t), at RH = 70% and T = 310 K. Stage I is characterised by a constant $\Delta T = \Delta T_{free,\ evap.}$ that is independent of d suggesting that free water evaporation from wet bauxite residue is sustained by rapid capillary flow. From the onset of stage II (at t = t_i), the surface temperature rises as evaporation becomes increasingly limited by slow gas phase diffusion until it reaches thermodynamic equilibrium (at t = t_f) with its environment at specific T and RH.

regimes for each sample thickness at 70% RH.

As drying kinetics slow down significantly with increasing RH, the distinct evaporation regimes can be most clearly observed, described and analysed under these more elevated RH conditions.

Experimental data obtained from the 6 mm thick sample at RH = 70 % (Figure 2E, green trace) is thus reproduced in Figure 3 in order to illustrate the most salient features used in the subsequent discussions and analysis. The time at which surface temperatures increase to $\Delta T = \Delta T_{free, evap.} + 30$ mK is used to signal the onset of the smooth transition between the stage I and stage II evaporation regimes and is indicated by the dashed vertical line labelled t_i, in Figure 3. Similarly, the diffusion-limited stage II evaporation regime can be considered complete when $\Delta T = -30$ mK, as indicated by the dotted vertical lines labelled t_f, in Figure 3. Using these somewhat arbitrary definitions, the duration of the diffusion-limited stage II evaporation regime in the thermograms of Figure 2 is observed to increase rapidly with sample thickness, and to decrease with RH.

At the end of stage II evaporation, bauxite residues samples reach a water content that should be nearly equilibrated with the ambient RH at the temperature of 310 K. In order to determine the water content within bauxite residues under equilibrium conditions, adsorption isotherm measurements were performed at each relative humidity by studying water uptake by initially dry bauxite residues samples (Figure 4). The adsorption isotherm indicates large water uptake by bauxite residues under these equilibrium conditions as expected from their large SSA while an important contribution must arise from their large microporosity.

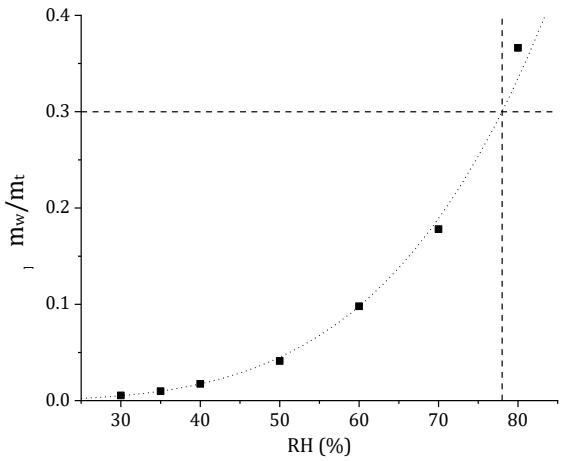

Figure 4. Adsorption isotherm of initially dry bauxite residues acquired at different RH at T = 310 K. The dotted line is a guide to the eye. The dashed lines highlight the fact that the equilibrium water content reaches 30 % (m_w/m_t) at RH = 78 %.

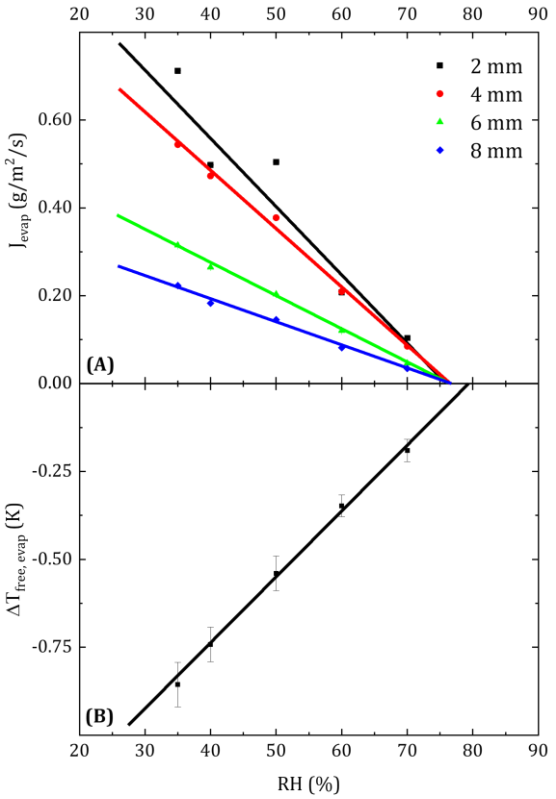

Figure 5. (A) Temperature difference in the initial stages of evaporation ($\Delta T_{free, evap.}$) as a function of relative humidity (RH). **(B)** Dependence of the average evaporation fluxes (J_{evap}) for each sample thickness [d = 2mm (black squares), 4mm (red circles), 6mm (green triangles), 8mm (blue diamonds)] as a function of relative humidity.

From the initial and equilibrium water contents, the loss of water experienced during the evaporation process could be calculated. Using the total mass of water evaporated from the samples, their total evaporation time (i.e., t_f), and the sample cross section (48 ± 2 mm^2), the

233 average evaporation fluxes, J_{evap}, from the bauxite residue samples could be calculated at the
234 specific RH and d of each experiment (Figure 5A). Inspection of the dependence of J_{evap} on RH
235 for each sample thickness (i.e., d = 2, 4, 6, and 8 mm labeled by black squares, red circles, green
236 triangle, and blue diamonds, respectively) provides important phenomenological information. J_{evap}
237 decreases linearly with increasing RH and intercepts the x-axis at RH = (76 ± 4) % and that,
238 irrespective of the sample thickness. This indicates that the surface boundary conditions imposed
239 by the ambient RH levels control the evaporative flux and thus, the evaporation time. In addition,
240 the temperature difference due to free water evaporation in drying stage I ($\Delta T_{free,\ evap.}$), reported in
241 Figure 5B, follows a linear relationship with RH, in accord with expectations from equation 1, and
242 approaches zero when RH = (79 ± 4) %. The x-intercept values for Figure 5A and 5B are consistent
243 with the adsorption isotherm of Figure 4, where the dashed lines indicate that an equilibrium water
244 content of 30 % (m_w/m_t) is reached at RH = 78 %. Interestingly data from Figure 5A also reveals
245 that J_{evap} increases with decreasing d which can be explained by the fact that a larger fraction of
246 the water content lies at, or near, the surface of the thinner samples where free water evaporation
247 occurs, resulting in higher average drying rates. This dependence indicates that J_{evap} is not only
248 controlled by the boundary conditions, which depend on RH, but also by long-range vapour phase
249 diffusion which inhibits water transport from the vaporisation plane to the samples' surface,
250 through the depleted evaporated interfacial zone.

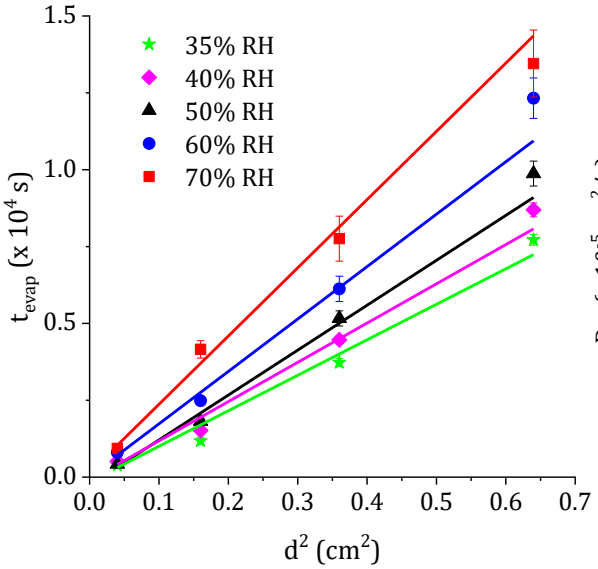

Figure 6. Stage II evaporation half-time (t_{evap}) as a function of the sample thickness squared (d^2) for RH = 35 % (green star), 40 % (magenta diamond), 50 % (black triangles), 60 % (blue circles), 70 % (red squares).

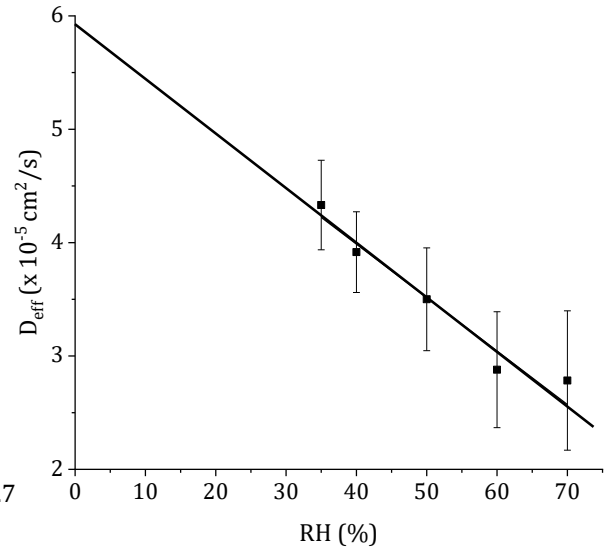

Figure 7. Dependence of the effective diffusion coefficient (D_{eff}) on the relative humidity (RH) at T = 310 K.

As stage II of the drying process is interpreted as being diffusion-limited, it is expected to follow Fick's law and to display an effective diffusion coefficient (D_{eff}). Diffusive transport would imply a linear dependence between diffusion time and the mean squared displacement of diffusing molecules whose slope could reveal the effective diffusion coefficient (D_{eff}), following $t_{evap} = \frac{d^2}{2D_{eff}}$, assuming 1D diffusive transport within the bauxite residues samples. Equating the mean squared displacement of diffusing molecules to the sample thickness [i.e., $\langle z^2 \rangle \sim d^2$], and using the stage II evaporation half-time (t_{evap}, defined here as $\frac{t_f - t_i}{2}$, using t_f and t_i as defined and displayed in Figure 3), Figure 6 shows that indeed, a linear relationship between t_{evap} and d^2 is obeyed. In addition to corroborating the diffusive nature of the rate limiting process for water

evaporation in late stage drying, an effective diffusion coefficient for water in bauxite residues can be obtained using linear fits to the experimental data in Figure 6.

The effective diffusion coefficients obtained at each RH are reported in Figure 7 and, interestingly, they decrease rapidly with increasing RH. Furthermore, these effective diffusion coefficients are four orders of magnitude smaller than those commonly measured for gas phase diffusion (Jabro, 2009). This must therefore reflect the fact that water diffusion is hindered by the microstructure and water adsorption propensity of the medium, properties that diminish the effective diffusion coefficient through the interstitial air within the bauxite residues interconnected porous microstructure. Indeed, when diffusive transport occurs in porous media, D_{eff} can be described using the molecular diffusion coefficient in air (D_{air}), the porosity of the sample (φ = 0.64 ± 0.06) and the tortuosity of its pore structure (τ = 1.38 ± 0.07) (Ho & Webb, 2006). Contributions arising from adsorption of water on pore surfaces are described using parameters that account for the water/bauxite residues interactions, namely an equilibrium constant for adsorption (K_{ads}), for the bauxite residues mass-to-pore volume ratio (r_{sp} = 0.7 ± 0.1 g/cm^3) and their specific surface area [SSA = (5 ± 1) x 10^5 cm^2/g] (Bartels-Rausch et al., 2013; Fabre, Barnola, Arnaud, & Chappellaz, 2000; Schwander et al., 1993; Seok et al., 2009):

$$D_{eff} = D_{air} \cdot \left(\frac{\varphi}{\tau}\right) \cdot \left(\frac{1}{1+ r_{sp} \times K_{ads} \times SSA}\right) \quad [3]$$

Equation 3 also provides a framework to understand the dependence of D_{eff} with RH. As the vaporisation plane leaves the surface of the bauxite residues, the overlying depleted zone, which remains in a quasi-steady state with the environmental conditions, acts as a diffusion barrier. When the RH increases, the water content in the evaporated interfacial layer, which is in a dynamic equilibrium with ambient air temperature and relative humidity, also increases. Consequently, the

air-filled porosity decreases, and the tortuosity of the pore structure increases, yielding a decrease in D_{eff} with increasing RH as observed in Figure 7.

Given that the morphological parameters, φ and τ, can only account for an utmost factor of $\frac{\varphi}{\tau} \sim 0.5$ reduction in D_{eff} compared to D_{air}, water adsorption on bauxite residue surfaces appears to be crucial in order to explain the smallness of D_{eff}. While SSA, r_{sp}, φ, and τ values are well established for dry bauxite residues (i.e., 0 % m_w/m_t), the equilibrium constant for adsorption, K_{ads}, for water for this material is unfortunately still unknown. A linear extrapolation of D_{eff} with RH enables the diffusion coefficient of water in dry bauxite residues to be estimated as D_{eff} = (5.9 ± 0.3) x 10^{-5} cm^2/s at RH = 0 %. Using Equation 3, along with the known morphological parameters of dry bauxite residues, a value for K_{ads} = (5 ± 1) x 10^{-3} cm is obtained. The magnitude of K_{ads} for bauxite tailings is observed to be greater than those reported for loam soils and alumina active F-200 for example, that is (6 ± 1) x 10^{-4} cm (Gary, Kohl, & Taylor, 1964) and (6.6 ± 0.9) x 10^{-5} cm (Serbezov, 2003), respectively. Therefore, water vapour strong propensity towards adsorption onto bauxite residues pore surfaces, along with their large SSA, are suggested to be the dominant contributors to the large decrease of D_{eff} compared to D_{air}, and the slow drying kinetics displayed in stage II evaporation regime.

CONCLUSIONS

Thermal imaging was demonstrated to be an efficient and innovative tool for monitoring surface evaporation from bauxite residues and establishing the underlying drying mechanisms. A thorough analysis of the experimental data enabled a deeper understanding of the evaporation kinetics and effective diffusion coefficients to be quantified. Water adsorption on bauxite residues

is demonstrated to be the dominant phenomenon in the rate-limiting mechanism in the later evaporation stage and to be responsible for the smallness of the effective diffusion coefficient. The evaporated interfacial layers therefore act as a diffusion barrier to water transport from the vaporization plane in the deeper layers of the bauxite residues to their surface, inhibiting considerably their drying rates.

A limitation of the thermal imaging approach is that it can only provide average evaporation fluxes. Indeed, as soon as the vaporization plane leaves the sample surface, contributions from the thermal gradient through the bauxite residues temperature depth profile arise, preventing instantaneous drying rates to be established and finer details in the evolution of the dominant water transport mechanisms to be elucidated. Concomitant gravimetric and thermal imaging measurements should provide us with further valuable mechanistic insight.

This methodology could also be expanded to environmental conditions relevant to field applications, namely the temperature dependence of the drying kinetics, especially those encountered under Winter conditions where capillary transport will be strongly suppressed (Feddes, Kabat, Van Bakel, Bronswijk, & Halbertsma, 1988). Environmental mitigation efforts could benefit greatly from improved understanding of the drying rates under such Winter condition where acute environmental consequences result from dust particles scattering from BRSA over snow-covered neighbouring urban communities (Aoki et al., 2006; Warren & Wiscombe, 1980). Collectively, these investigations should improve our ability to forecast and prevent the occurrence of fugitive dust emissions as well as to devise efficient risk assessment and monitoring tools to assist in mining residue management efforts.

ACKNOWLEDGEMENT

We thank the Fonds de recherche du Québec – Nature et Technologies (FRQNT), Rio Tinto Alcan Inc., Natural Sciences and Engineering Research Council of Canada (NSERC), Université de Sherbrooke – Faculté des sciences, ECO Canada and the Ministère de l'Énergie et des Ressources Naturelles (MERN) for grants supporting this work. We gratefully acknowledge Rio Tinto Alcan Inc. in Vaudreuil, Canada for providing bauxite residue samples, access to the BRSA and technical support. We would also like to acknowledge anonymous reviewers for their valuable comments and suggestions. Data archiving is underway

AUTHOR INFORMATION

Corresponding Author

Josée Maurais: Josee.Maurais@USherbrooke.ca

350 REFERENCES

351

352 Allan, R. J. (1995). Impact of Mining Activities on the Terrestrial and Aquatic Environment with
353 Emphasis on Mitigation and Remedial Measures. In U. Förstner, W. Salomons, & P. Mader
354 (Eds.), *Heavy Metals* (pp. 119–140). Springer, Berlin, Heidelberg.
355 https://doi.org/10.1007/978-3-642-79316-5_8

356 Amano, E., & Salvucci, G. D. (1989). Detection and Use of Three Signatures of Soil-Limited
357 Evaporation. *Remote Sensing of Environment*, *4257*(98).

358 Aoki, T., Motoyoshi, H., Kodama, Y., Yasunari, T. J., Sugiura, K., & Kobayashi, H. (2006).
359 Atmospheric Aerosol Deposition on Snow Surfaces and Its Effect on Albedo. *SOLA*, *2*, 13–
360 16. https://doi.org/10.2151/sola.2006-004

361 Bartels-Rausch, T., Wren, S. N., Schreiber, S., Riche, F., Schneebeli, M., & Ammann, M. (2013).
362 Diffusion of volatile organics through porous snow: impact of surface adsorption and grain
363 boundaries. *Atmospheric Chemistry and Physics*, *13*(14), 6727–6739.
364 https://doi.org/10.5194/acp-13-6727-2013

365 Brevik, E. C., Fenton, T. E., & Lazari, A. (2006). Soil electrical conductivity as a function of soil
366 water content and implications for soil mapping. *Precision Agriculture*, *7*(6), 393–404.
367 https://doi.org/10.1007/s11119-006-9021-x

368 Bristow, K. L. (1998). Measurement of thermal properties and water content of unsaturated sandy
369 soil using dual-probe heat-pulse probes. *Agricultural and Forest Meteorology*, *89*(2), 75–84.
370 https://doi.org/10.1016/S0168-1923(97)00065-8

Bristow, K. L., Campbell, G. S., & Calissendorff, K. (1993). Test of a Heat-Pulse Probe for Measuring Changes in Soil Water Content. *Soil Science Society of America Journal*, *57*, 930–934. https://doi.org/10.2136/sssaj1993.03615995005700040008x

Fabre, A., Barnola, J.-M., Arnaud, L., & Chappellaz, J. (2000). Determination of gas diffusivity in polar firn: Comparison between experimental measurements and inverse modeling. *Geophysical Research Letters*, *27*(4), 557–560. https://doi.org/10.1029/1999GL010780

Feddes, R. A., Kabat, P., Van Bakel, P. J. T., Bronswijk, J. J. B., & Halbertsma, J. (1988). Modelling soil water dynamics in the unsaturated zone — State of the art. *Journal of Hydrology*, *100*(1), 69–111. https://doi.org/10.1016/0022-1694(88)90182-5

Fuchs, M., & Tanner, C. B. (1967). Evaporation from a Drying Soil. *Journal of Applied Meteorology*, *6*(5), 852–857. https://doi.org/10.1175/1520-0450(1967)006<0852:EFADS>2.0.CO;2

Gary, J. W., Kohl, R. A., & Taylor, S. A. (1964). Water Adsorption by Dry Soil and Its Thermodynamic Functions. *Soil Science Society Proceedings*, *28*(3), 309–314. https://doi.org/doi:10.2136/sssaj1964.03615995002800030007x

Griend, A. A., & Owe, M. (1994). Bare soil surface resistance to evaporation by vapor diffusion under semiarid conditions. *Water Resources Research*, *30*(2), 181–188. https://doi.org/10.1029/93WR02747

Grifoll, J., Gastó, J. M., & Cohen, Y. (2005). Non-isothermal soil water transport and evaporation. *Advances in Water Resources*, *28*(11), 1254–1266. https://doi.org/10.1016/j.advwatres.2005.04.008

Ho, C. K., & Webb, S. W. (2006). *Gas Transport in Porous Media*. Springer Netherlands. https://doi.org/10.1007/1-4020-3962-X

Hopmans, J. W., Šimunek, J., & Bristow, K. L. (2002). Indirect estimation of soil thermal properties and water flux using heat pulse probe measurements: Geometry and dispersion effects. *Water Resources Research*, *38*(1), 7–14. https://doi.org/10.1029/2000WR000071

Jabro, J. D. (2009). Water Vapor Diffusion Through Soil as Affected by Temperature and Aggregate Size. *Transport in Porous Media*, *77*(3), 417–428. https://doi.org/10.1007/s11242-008-9267-z

Kosky, P., Balmer, R., Keat, W., & Wise, G. (2013). Chapter 12 - Mechanical Engineering. In P. Kosky, R. Blamer, W. Keat, & G. Wise (Eds.), *Exploring Engineering* (Third Edit, pp. 259–281). Boston: Academic Press. https://doi.org/10.1016/B978-0-12-415891-7.00012-1

Li, L. Y. (1998). Properties of red mud tailings produced under varying process conditions. *Journal of Environmental Engineering*, *124*(3), 254–264. https://doi.org/10.1061/(ASCE)0733-9372(1998)124:3(254)

Li, L. Y. (2001). A study of iron mineral transformation to reduce red mud tailings. *Waste Management*, *21*(6), 525–534. https://doi.org/10.1016/S0956-053X(00)00107-0

Li, L. Y., & Rutherford, G. K. (1996). Effect of bauxite properties on the settling of red mud. *International Journal of Mineral Processing*, *48*(3–4), 169–182. https://doi.org/10.1016/S0301-7516(96)00024-5

Maurais, J., Bourret, J., Dauphinais, E., Larivière-Loiselle, C., Beaumont, É., Morin, É., … Ayotte, P. (2018). Prevention And Mitigation Of Fugitive Dust Emission From Bauxite Residue:

Aggravating Environmental Effects, Forecasting And Risk Assessment. In *Alumina Quality Workshop (AQW) 2018*. Gladstone: Alumina Quality Workshop (AQW).

McKenna Neuman, C., Boulton, J. W., & Sanderson, S. (2009). Wind tunnel simulation of environmental controls on fugitive dust emissions from mine tailings. *Atmospheric Environment*, *43*(3), 520–529. https://doi.org/10.1016/j.atmosenv.2008.10.011

Moldrup, P., Olesen, T., Komatsu, T., Schjønning, P., & Rolston, D. E. (2001). Tortuosity, Diffusivity, and Permeability in the Soil Liquid and Gaseous Phases. *Soil Science Society of America Journal*, *65*, 613–623. https://doi.org/10.2136/sssaj2001.653613x

Monteith, J. L. (1981). Evaporation and surface temperature. *Quarterly Journal of the Royal Meteorological Society*, *107*(451), 1–27. https://doi.org/10.1002/qj.49710745102

Neriah, A. Ben, Assouline, S., Shavit, U., & Weisbrod, N. (2014). Impact of ambient conditions on evaporation from porous media. *Water Resources Research*, *50*(8), 6696–6712. https://doi.org/10.1002/2014WR015523

Or, D., Lehmann, P., Shahraeeni, E., & Shokri, N. (2006). Advances in Soil Evaporation Physics — A Review. *Vadose Zone Journal*, *12*(4). https://doi.org/10.2136/vzj2012.0163

Pfister, L., McDonnell, J. J., Hissler, C., & Hoffmann, L. (2010). Ground-based thermal imagery as a simple, practical tool for mapping saturated area connectivity and dynamics. *Hydrological Processes*, *24*(21), 3123–3132. https://doi.org/10.1002/hyp.7840

Power, G., Gräfe, M., & Klauber, C. (2011). Bauxite residue issues: I. Current management, disposal and storage practices. *Hydrometallurgy*, *108*(1–2), 33–45. https://doi.org/10.1016/j.hydromet.2011.02.006

Price, J. C. (1980). The potential of remotely sensed thermal infrared data to infer surface soil moisture and evaporation. *Water Resources Research*, *16*(4), 787–795. https://doi.org/10.1029/WR016i004p00787

Saravanapavan, T., & Salvucci, G. D. (2000). Analysis of rate-limiting processes in soil evaporation with implications for soil resistance models. *Advances in Water Resources*, *23*, 493–502. https://doi.org/10.1016/S0309-1708(99)00045-7

Schwander, J., Barnola, J.-M., Andrié, C., Leuenberger, M., Ludin, A., Raynaud, D., & Stauffer, B. (1993). The age of the air in the firn and the ice at Summit, Greenland. *Journal of Geophysical Research: Atmospheres*, *98*(D2), 2831–2838. https://doi.org/10.1029/92JD02383

Seok, B., Helmig, D., Williams, M. W., Liptzin, D., Chowanski, K., & Hueber, J. (2009). An automated system for continuous measurements of trace gas fluxes through snow: an evaluation of the gas diffusion method at a subalpine forest site, Niwot Ridge, Colorado. *Biogeochemistry*, *95*(1), 95–113. https://doi.org/10.1007/s10533-009-9302-3

Serbezov, A. (2003). Adsorption Equilibrium of Water Vapor on F-200 Activated Alumina. *Journal of Chemical & Engineering Data*, *48*(2), 421–425. https://doi.org/10.1021/je025616d

Shahraeeni, E., & Or, D. (2010). Thermo-evaporative fluxes from heterogeneous porous surfaces resolved by infrared thermography. *Water Resources Research*, *46*(9).

Shao, Y. (2001). A model for mineral dust emission. *Journal of Geophysical Research: Atmospheres*, *106*(D17), 20239–20254. https://doi.org/10.1029/2001JD900171

455 Sheets, K. R., & Hendrickx, J. M. H. (1995). Noninvasive Soil Water Content Measurement Using
456 Electromagnetic Induction. *Water Resources Research*, *31*(10), 2401–2409.
457 https://doi.org/10.1029/95WR01949

458 Shokri, N., Lehmann, P., & Or, D. (2009). Critical evaluation of enhancement factors for vapor
459 transport through unsaturated porous media. *Water Resources Research*, *45*, 1–9.
460 https://doi.org/10.1029/2009WR007769

461 Shokri, N., & Or, D. (2011). What determines drying rates at the onset of diffusion controlled
462 stage-2 evaporation from porous media ? *Water Resources Research*, *47*, 1–8.
463 https://doi.org/10.1029/2010WR010284

464 Teng, J., Zhang, X., Zhang, S., Zhao, C., & Sheng, D. (2019). An analytical model for evaporation
465 from unsaturated soil. *Computers and Geotechnics*, *108*, 107–116.
466 https://doi.org/10.1016/j.compgeo.2018.12.005

467 Thiery, J., Rodts, S., Weitz, D. A., & Coussot, P. (2017). Drying regimes in homogeneous porous
468 media from macro- to nanoscale. *Phys. Rev. Fluids*, *2*(7), 74201.
469 https://doi.org/10.1103/PhysRevFluids.2.074201

470 Topp, G. C., & Davis, J. L. (1985). Measurement of Soil Water Content using Time-domain
471 Reflectrometry (TDR): A Field Evaluation. *Soil Science Society of America Journal*, *49*, 19–
472 24. https://doi.org/10.2136/sssaj1985.03615995004900010003x

473 Van Dam, R. L. (2014). Calibration Functions for Estimating Soil Moisture from GPR Dielectric
474 Constant Measurements. *Communications in Soil Science and Plant Analysis*, *45*(3), 392–
475 413. https://doi.org/10.1080/00103624.2013.854805

476 Wang, J. C., Xia, Z. Q., Wang, J. X., & Lu, Z. H. (2012). Field Evaluation of 12 Soil Moisture
477 Sensors on a Sandy Loam Soil in Lu'an, Subtropical Monsoon Climate Region, China.
478 *Advanced Materials Research*, *482–484*, 372–375.
479 https://doi.org/10.4028/www.scientific.net/AMR.482-484.372

480 Warren, S. G., & Wiscombe, W. J. (1980). A Model for the Spectral Albedo of Snow. II: Snow
481 Containing Atmospheric Aerosols. *Journal of the Atmospheric Sciences*, *37*(12), 2734–2745.
482 https://doi.org/10.1175/1520-0469(1980)037<2734:AMFTSA>2.0.CO;2

483 Yu, X., & Drnevich, V. P. (2004). Soil Water Content and Dry Density by Time Domain
484 Reflectometry. *Journal of Geotechnical and Geoenvironmental Engineering*, *130*(9), 922–
485 934. https://doi.org/10.1061/(ASCE)1090-0241(2004)130:9(922)

486